





Tripartite quantum Rabi model with trapped Rydberg ions

Thomas J. Hamlyn ^{1,2} Chi Zhang ³ Igor Lesanovsky ^{4,1,2} and Weibin Li ^{1,2}

¹*School of Physics and Astronomy, University of Nottingham, Nottingham NG7 2RD, United Kingdom*

²*Centre for the Mathematics and Theoretical Physics of Quantum Non-Equilibrium Systems, University of Nottingham, Nottingham NG7 2RD, United Kingdom*

³*Division of Physics, Mathematics, and Astronomy, California Institute of Technology, Pasadena, California 91125, USA*

⁴*Institut für Theoretische Physik, Universität Tübingen, Auf der Morgenstelle 14, 72076 Tübingen, Germany*



(Received 3 January 2024; accepted 19 April 2024; published 31 May 2024)

We investigate a tripartite quantum Rabi model (TQRM) wherein a bosonic mode concurrently couples to two spin-1/2 particles through a spin-spin interaction, resulting in a spin-spin-boson coupling—a departure from conventional quantum Rabi models featuring bipartite spin-boson couplings. The symmetries of the TQRM depend on the detuning parameter, representing the energy difference between the spin states. At zero detuning a parity symmetry renders the TQRM reducible to a quantum Rabi model. A subradiant-to-superradiant transition in the ground state is predicted as the tripartite coupling strength increases. For nonzero detuning the total spin emerges as the sole conserved quantity in the TQRM. It is found that superradiance prevails in the ground state as long as the tripartite coupling remains nonzero. We derive the Braak \mathcal{G} function of the TQRM analytically, with which the eigenspectra are obtained. The TQRM can be realized in a viable trapped Rydberg ion quantum simulator, where the required tripartite couplings and single-body interactions in the TQRM are naturally present. Our study opens opportunities to explore and create correlations and entanglement in the spin and motional degrees of freedoms with the TQRM.

DOI: [10.1103/PhysRevResearch.6.023223](https://doi.org/10.1103/PhysRevResearch.6.023223)

I. INTRODUCTION

The quantum Rabi model (QRM) consists of a spin-1/2 particle coupled to a bosonic degree of freedom [1]. Despite its simplicity, the QRM exhibits rich physics [2] and finds applications in, e.g., benchmarking quantum computers [3], verifying the existence of supersymmetric quantum mechanics [4,5], investigating \mathcal{PT} -symmetry breaking [6,7], and the generation of nonclassical states [8,9]. An important feature of the QRM is that the validity of the rotating wave approximation breaks down as a result of the strong spin-boson coupling [10–12]. This causes difficulties in obtaining the spectrum of the QRM analytically. Such a task was not accomplished until 2011 by Braak [13] through the \mathcal{G} -function method, although the isolated doubly degenerate energies that represent the exceptional spectrum were analytically determined decades earlier [14]. After this achievement, many studies have focused on understanding the mathematical structure and improving the numerical stability and performance of the \mathcal{G} function [15–20]. When the coupling is strong the ground state of the QRM exhibits a superradiant-like phase transition, where the population of the boson becomes sizable when increasing the coupling above a critical value [21–24]. Motivated by the rich physics, the QRM has been experimentally

realized with various physical systems [20], including trapped ions [25,26], cavity and circuit QED [27–33], cavity optomechanics [34], and quantum dots [35,36]. Furthermore, superradiant transition has been experimentally demonstrated with a single trapped ion [26].

Modified QRMs have been extensively explored within the literature [20]. The first type of extension concerns the modification of the bosonic operators. For example, two-photon QRMs, where the spin couples to the bosonic mode via a two-photon process, have attracted a lot of attention [19,37–42]. The symmetry extends from a \mathbb{Z}_2 group in the QRM to a \mathbb{Z}_4 group in the two-photon QRM [38]. Despite the change of symmetry, the spectra of the two-photon QRM can still be found analytically [43,44]. Another way to extend the QRM is to include more spins in the model, such as two-qubit QRMs (TQQRMs) [45–56]. Such extension leads to the Dicke model when the number of spins is large [57]. However, all of these existing studies have focused on bipartite couplings which couple individual spins with bosonic modes.

In this article we study an exotic tripartite quantum Rabi model (TQRM) where two identical spins couple to a monochromatic bosonic mode simultaneously through an Ising spin-spin interaction. To the best of our knowledge, such extension has not been studied before. Three- and multi-body interactions have attracted a broad interest in the study of nuclear, atomic, and many-body physics [58]. Recent experimental and theoretical studies have realized multibody interactions with trapped ions [59], neutral atoms [60], and superconducting circuits [61,62]. A key feature of the TQRM is that the constituents of the TQRM are a bosonic mode

Published by the American Physical Society under the terms of the [Creative Commons Attribution 4.0 International license](https://creativecommons.org/licenses/by/4.0/). Further distribution of this work must maintain attribution to the author(s) and the published article's title, journal citation, and DOI.

and two identical spins. We show that the TQRM can be realized with two trapped ions in their highly excited Rydberg electronic states [63,64]. In a linear Paul trap long-range dipole-dipole interactions between Rydberg ions couple to the breathing mode of a two-ion crystal [65], leading to the tripartite coupling between the two spins and bosonic mode (crystal phonons). The TQRM is achieved through modulating the Rydberg excitation and phonon-ion coupling with external laser fields.

The symmetries of the TQRM are controlled by the Rydberg excitation laser. At vanishing detuning the TQRM has a well-defined parity symmetry that relies on the total population of the spins and phonon. When the detuning is finite, the parity symmetry disappears. We derive analytically the \mathcal{G} function that defines the eigenspectrum of the TQRM, and show that these analytical results indeed match those of numerical calculations. We then investigate the ground-state properties, focusing on the strong coupling regime. At zero detuning the TQRM reduces to an effective QRM, which differs from the QRM insofar as it describes a collective interaction between the spins and the bosonic mode. In the superradiant phase the spatial distribution of the phonon splits into two peaks symmetrically, and its state is captured by a classical mixture of two coherent states $|\pm\alpha\rangle$ ($\alpha > 0$). At finite detuning the superradiance gradually dominates the ground state. It is found that the phonon spatial distribution has a single peak, which is shifted from the origin in the strong coupling regime. A careful examination shows that the phonon state is approximately described by coherent state $|\alpha\rangle$.

This article is organized as follows. In Sec. II we present the trapped ion system used as the quantum simulator and derive the TQRM Hamiltonian. In Sec. III we discuss the symmetries present in the model and how the single-spin detuning affects the symmetry. The \mathcal{G} function is derived analytically in Sec. IV. In Sec. V we discuss superradiance and the phase space distribution function of phonons in the ground state of the TQRM. We conclude in Sec. VI.

II. TRIPARTITE QUANTUM RABI MODEL WITH A PAIR OF TRAPPED RYDBERG IONS

In this section we provide details on how to realize the TQRM with a Rydberg ion quantum simulator. We consider trapped ions excited to highly excited electronic states with principal quantum number $n \gg 1$. Trapped Rydberg ions exhibit exaggerated properties compared to the ground state [66,67], such as long lifetime [68], strong and controllable two-body interactions [64], and strong coupling between vibrational (phonon) and electronic states [69–74]. As a consequence of the tunable nature of these properties, trapped Rydberg ions have been proposed as analog and digital quantum computers [64,66,71–73], platforms for investigating mesoscopic physics [75], exploring topological physics [74], and vibronic coupling [76]. Recently, Rydberg excitation of $^{88}\text{Sr}^+$ and $^{40}\text{Ca}^+$ ions and entangling gates with trapped Rydberg ions [64] have been achieved experimentally [77–83].

In our setting two ions are trapped in a linear Paul trap, as depicted in Fig. 1(a). Due to the harmonic trapping potential (axial trapping frequency ν) and Coulomb repulsion,

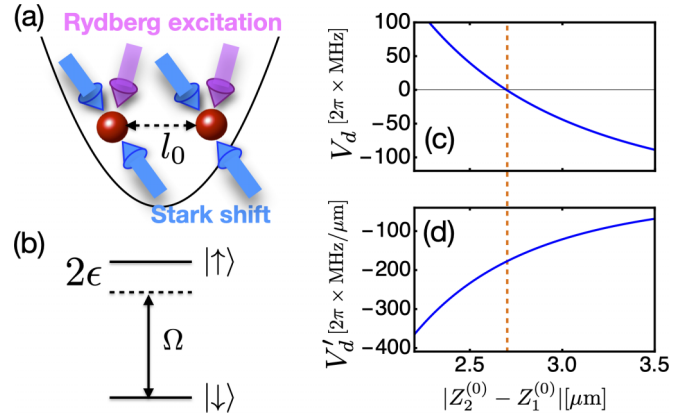


FIG. 1. (a) Two ions are confined in a linear Paul trap with trap frequency ν . The ions are coherently laser excited to Rydberg states. In their Rydberg states the ions interact through dipolar interaction depending on their separation $l_0 = |Z_2^{(0)} - Z_1^{(0)}|$. A standing wave laser field (blue arrows) induces a site-dependent Stark shift. (b) The Rydberg excitation laser excites the ions from the ground state $|\downarrow\rangle$ to the Rydberg state $|\uparrow\rangle$ with Rabi frequency Ω and detuning 2ϵ . (c) The dipolar interaction. At $l_0 = 2.7$ μm the interaction $V_d(l_0) = 0$ (marked by the dashed perpendicular line). (d) The slope V'_d of the dipolar interaction. $V'_d = -2\pi \times 174.7$ MHz/ μm when $l_0 = 2.7$ μm . The dipolar interaction is induced through using the microwave-dressed Rydberg states [74]. In this example, we have considered $^{88}\text{Sr}^+$ with principal quantum number $n = 80$, and $\nu = 2\pi \times 2.02$ MHz. See text for details.

the two ions form a Wigner crystal along the trap axis (z axis) at low temperatures, where coordinates of the j th ion are X_j, Y_j , and Z_j ($j = 1, 2$). The ions vibrate around their equilibrium positions $X_j^{(0)} = Y_j^{(0)} = 0$ and $Z_2^{(0)} = -Z_1^{(0)} = (\mathcal{N}^2 e^2 / 16\pi \epsilon_0 M \nu)^{1/3}$, where $\mathcal{N}e$ is the net charge, M the mass of the ion, and ϵ_0 the permittivity of free space. As we will show later, the electronic states (spin) will couple to the axial vibration, while the radial motions will not be involved. Along the trap axis we obtain a center-of-mass (c.m.) and breathing modes whose frequencies are $\omega_{\text{c.m.}} = \nu$ and $\omega = \sqrt{3}\nu$, respectively [65]. A Rydberg excitation laser couples the low-energy metastable state $|\downarrow\rangle = |4D_{5/2}\rangle$ and a Rydberg state $|\uparrow\rangle$ (e.g., $|nS_{1/2}\rangle$ with n the principal quantum number) coherently [63]. At the same time an off-resonant standing wave laser induces a state-dependent Stark shift F_j [84,85]. The Hamiltonian of the system reads ($\hbar \equiv 1$),

$$H_t = \omega_{\text{c.m.}} a_{\text{c.m.}}^\dagger a_{\text{c.m.}} + \omega a^\dagger a + \sum_{j=1,2} (\Omega \sigma_j^x + \epsilon \sigma_j^z + F_j) + H_d,$$

where $a_{\text{c.m.}}^\dagger$ ($a_{\text{c.m.}}$) and a^\dagger (a) are the creation (annihilation) operators of the c.m. and breathing mode, respectively. The operators σ_j^x , σ_j^z , and $n_j = \frac{1}{2}(1 + \sigma_j^z)$ are Pauli and projection operators of the j th ion. Ω and ϵ are the Rabi frequency and detuning. F_j describes the Stark shift due to the standing wave laser. In Rydberg states the ions interact via a dipole-dipole interaction $H_d = V_d(Z_2 - Z_1)n_1 n_2$ with the distance-dependent strength $V_d(Z_2 - Z_1)$ [64,71].

At low temperatures the characteristic length of the c.m. and breathing vibrations are $l_{\text{c.m.}} = 1/\sqrt{2M\nu}$ and $l_b = 1/\sqrt{2M\omega}$, respectively. For typical trap parameters, the length

is in the order of a few tens of nanometers, while the distance between the two ions is several micrometers [64,65]. This allows us to expand $V_d(Z_2 - Z_1)$ around their equilibrium positions. To the linear order of Z_j , we obtain $V_d(Z_2 - Z_1) \approx V_d(l_0) + V'_d(l_0)(z_2 - z_1)$, where $V_d(l_0)$ and $V'_d(l_0)$ are the potential and its slope at the equilibrium distance $l_0 = |Z_2^{(0)} - Z_1^{(0)}|$. z_j is the small deviation from the equilibrium position $Z_j^{(0)}$. By modulating the Rydberg states with external microwave fields we can tune $V_d(l_0) = 0$, i.e., the dipolar interaction vanishes at the equilibrium distance, as shown in Refs. [73,74]. See Figs. 1(c) and 1(d) for an example. As a result, the dipolar interaction couples directly to the breathing mode through $V_d(Z_1 - Z_2) \approx G(a^\dagger + a)$, where $G = l_0 V'_d(l_0)$ gives the coupling strength. Note that the c.m. mode decouples with the electronic dynamics. We will exclusively focus on the coupled dynamics between the spin and breathing mode from now on.

With the above consideration one obtains $H_d \approx g(\sigma_1^z \sigma_2^z + \sigma_1^z + \sigma_2^z + 1)(a + a^\dagger)$, with $g = G/4$. Our aim is to achieve a spin-spin-phonon coupled interaction $\propto \sigma_1^z \sigma_2^z (a + a^\dagger)$. To achieve this, one can turn off the coupling between the individual spin and phonon through the spin-dependent Stark shift [84] with $F_1 = -g(\sigma_1^z + 1/2)(a + a^\dagger)$ and $F_2 = -g(\sigma_2^z + 1/2)(a + a^\dagger)$. Details of the implementation can be found in Appendix. The only remaining term is a collective coupling between the two spins and phonon, i.e., the breathing mode couples to the two spins simultaneously, whose strength depends on the slope of the two-body dipolar interaction. This yields the Hamiltonian

$$H = \omega a^\dagger a + \Omega(\sigma_1^x + \sigma_2^x) + \epsilon(\sigma_1^z + \sigma_2^z) + g(a^\dagger + a)\sigma_1^z \sigma_2^z. \quad (1)$$

Equation 1 represents the TQRM consisting of a monochromatic bosonic (phonon) mode of frequency ω and two identical spins. The unique aspect of the TQRM compared to the QRM and its variants previously studied is that our model is characterized by a tripartite coupling, i.e., a spin-spin-boson coupling. The tripartite coupling is different from existing models. In conventional multispin QRMs the two-body interactions between spins are typically not present (see Refs. [45–54]), or the spin-spin interactions do not directly couple to the bosonic mode [55,56].

III. SYMMETRIES OF THE TQRM

We begin by examining symmetries in the TQRM and how the single-body detuning affects the symmetries. It is convenient to rotate the Hamiltonian (1) around the σ_i^y axes by $\pi/2$, yielding

$$H_R = \omega a^\dagger a - \Omega(\sigma_1^z + \sigma_2^z) + \epsilon(\sigma_1^x + \sigma_2^x) + g\sigma_1^x \sigma_2^x (a^\dagger + a). \quad (2)$$

In the rotated basis the spin-up and spin-down states will be denoted with $|\uparrow\rangle$ and $|\downarrow\rangle$, respectively. After the rotation, both the detuning and the tripartite coupling term of H_R can induce transitions between spin states. In the following, we first analyze symmetries in the TQRM when the Rydberg excitation laser is resonant ($\epsilon = 0$), where transition between states is solely driven by the tripartite coupling. Next, we consider finite detuning ($\epsilon \neq 0$), where both terms will be taken into account.

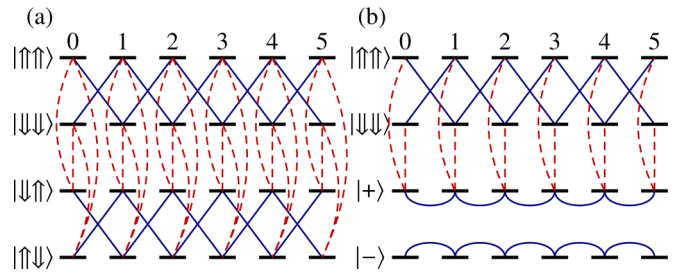


FIG. 2. Coupling between different spin-phonon states. (a and b) Coupling with basis $\{|\uparrow\uparrow, n\rangle, |\downarrow\downarrow, n\rangle, |\uparrow\downarrow, n\rangle, |\downarrow\uparrow, n\rangle\}$ and $\{|\uparrow\uparrow, n\rangle, |\downarrow\downarrow, n\rangle, |+, n\rangle, |-, n\rangle\}$, respectively. Solid lines show transitions between the basis induced solely by the tripartite coupling. This is the only coupling in the resonant TQRM (i.e., $\epsilon = 0$). When $\epsilon \neq 0$, additional transitions are induced by the single-body coupling, indicated by dashed lines.

A. Resonant TQRM

When $\epsilon = 0$, the spin states of the two ions are only coupled through the tripartite interaction, i.e., via the $\sigma_1^x \sigma_2^x$ term. The double-spin-down state $|\downarrow\downarrow\rangle$ can only couple to the $|\uparrow\uparrow\rangle$ state, i.e., $\sigma_1^x \sigma_2^x |\uparrow\uparrow\rangle = |\downarrow\downarrow\rangle$, and vice versa. Here, $|s_1 s_2\rangle = |s_1\rangle \otimes |s_2\rangle$ with the spin state $|s_j\rangle$ ($s_j = \{\uparrow, \downarrow\}$). A similar transition can be found between states $|\uparrow\downarrow\rangle$ and $|\downarrow\uparrow\rangle$. This shows that the two sectors $\{|\uparrow\uparrow\rangle, |\downarrow\downarrow\rangle\}$ and $\{|\uparrow\downarrow\rangle, |\downarrow\uparrow\rangle\}$ are separable (e.g., block diagonal), and hence can be treated individually.

As there are two spin states in sector $\{|\uparrow\uparrow\rangle, |\downarrow\downarrow\rangle\}$, we define collective spin operators $S^z = |\uparrow\uparrow\rangle\langle\uparrow\uparrow| - |\downarrow\downarrow\rangle\langle\downarrow\downarrow|$ and $S^x = |\uparrow\uparrow\rangle\langle\downarrow\downarrow| + |\downarrow\downarrow\rangle\langle\uparrow\uparrow|$. Then, we project Hamiltonian (2) to this subspace, yielding

$$H_s = \omega a^\dagger a - 2\Omega S^z + g S^x (a^\dagger + a).$$

Thus, TQRM is equivalent to the conventional QRM in this sector. However, due to the collective nature the effective level separation becomes 4Ω , and the phonon mode couples electronic states of the two spins. In this regime H_s exhibits a parity symmetry with parity operator $\Pi_p = \exp(i\pi N_E)$ [13], with the total excitation $N_E = a^\dagger a + S^z$. Its eigenvalues are 1 (−1) when N_E is an even (odd) integer. It can be shown that $\Pi_p H_s \Pi_p^\dagger = H_s$. Such parity, as depicted in Fig. 2(a), requires that when spin states change, phonon state $|n\rangle$ changes to $|n \pm 1\rangle$.

In spin sector $\{|\uparrow\downarrow\rangle, |\downarrow\uparrow\rangle\}$, we note that $-\Omega(\sigma_1^z + \sigma_2^z)$ is removed from Hamiltonian H_R as one obtains zero eigenvalue when applying this term on the spin states $\{|\uparrow\downarrow\rangle, |\downarrow\uparrow\rangle\}$. Hamiltonian H_R is simplified to be $H'_R = \omega a^\dagger a + g\sigma_1^x \sigma_2^x (a^\dagger + a)$. The coupling in this basis is depicted in Fig. 2(a) (lower panel, solid lines). By defining superposition basis $|\pm\rangle = \frac{1}{\sqrt{2}}(|\uparrow\downarrow\rangle \pm |\downarrow\uparrow\rangle)$, Hamiltonian H'_R becomes diagonal in this basis, leading to $H_\pm = \omega a^\dagger a \pm g(a^\dagger + a)$, where + (−) corresponds to the superposition state $|+\rangle$ ($|-\rangle$). In each superposition state $|\pm\rangle$, phonon states $|n\rangle$ couple to $|n \pm 1\rangle$ without affecting the spin state, as depicted in Fig. 2(b). Hamiltonian H_\pm describes displaced harmonic oscillators, whose eigenenergies, $E_\pm(n) = n\omega - g^2/\omega$, are double degenerate at a given n [86].

B. Detuned TQRM

For finite detuning, i.e., $\epsilon \neq 0$, H_R induces transitions between states $|s_1 s_2, n\rangle$ through both the tripartite coupling and σ_j^x operators. These couplings are shown with solid and dashed lines in Fig. 2(a), respectively. The total spin operator $\mathbf{S} = (\mathbf{s}_1 + \mathbf{s}_2)$ is a conserved quantity with $\mathbf{s}_j = \sigma_j^x + \sigma_j^y + \sigma_j^z$. By defining the triplet manifold $\{|\uparrow\uparrow\rangle, |+\rangle, |\downarrow\downarrow\rangle\}$ and singlet manifold $|-\rangle$, one finds that the two manifolds decouple. This can be seen in Fig. 2(b). The Hamiltonian of the singlet manifold is H_- , whose eigenenergy $E_-(n)$ is independent of the spin degrees of freedom.

IV. ENERGY SPECTRUM

Eigenspectra of many variants of QRMs have been obtained analytically [20], typically through the Braak \mathcal{G} function. The \mathcal{G} functions are derived either through a transformation into the Segal-Bargmann space of complex analytic functions [87], or through the Bogoliubov operator approach (BOA) introduced by Chen *et al.* [44]. We will employ the BOA, as it generates algebraically simpler \mathcal{G} functions than the Segal-Bargmann approach [44,48,51]. When $\epsilon = 0$, our model reduces to an effective QRM, whose analytical spectrum is known [13]. In the following we will focus on the spectrum of Hamiltonian (1) in the triplet sector for $\epsilon \neq 0$.

A. Bogoliubov transformation and the Braak \mathcal{G} function

To diagonalize H in the spin triplet manifold, we define two sets of Bogoliubov operators $A = a + g/\omega$ and $B = a - g/\omega$.

They are shifted bosonic operators and fulfill the commutation relation of bosonic operators, i.e., $[\xi, \xi^\dagger] = 1$ and $[\xi, \xi] = [\xi^\dagger, \xi^\dagger] = 0$ ($\xi = A, B$). They act on the Fock states $|n_A\rangle = (A^\dagger)^n |0_A\rangle/\sqrt{n!}$ and $|n_B\rangle = (B^\dagger)^n |0_B\rangle/\sqrt{n!}$, respectively. Note that $|0_\xi\rangle$ ($\xi = A, B$) is a displaced phonon vacuum state $|0\rangle$ of Hamiltonian (1),

$$|0_\xi\rangle = \exp\left(-\frac{1}{2}\left(\frac{g}{\omega}\right)^2 \mp \frac{ga^\dagger}{\omega}\right)|0\rangle, \tag{3}$$

i.e., $|0_\xi\rangle$ is a coherent state, where the sign is $-(+)$ when $\xi = A$ ($\xi = B$). The relation between the coherent states $|0_\xi\rangle$ [88] and $|0\rangle$ is important in a later step of our derivation.

Using the Bogoliubov operators A and A^\dagger , and in the triplet manifold, the Hamiltonian H can be written as

$$H_A = \begin{bmatrix} \mathcal{F}_A + 2\epsilon & \sqrt{2}\Omega & 0 \\ \sqrt{2}\Omega & \mathcal{D}_A & \sqrt{2}\Omega \\ 0 & \sqrt{2}\Omega & \mathcal{F}_A - 2\epsilon \end{bmatrix}, \tag{4}$$

where $\mathcal{F}_A = \omega A^\dagger A - g^2/\omega$ and $\mathcal{D}_A = \omega A^\dagger A - 2g(A^\dagger + A) + 3g^2/\omega$. Next, we expand the eigenstate $|\Psi_A\rangle$ of H_A with

$$|\Psi_A\rangle = \begin{bmatrix} \sum_{n=0}^\infty \sqrt{n!} c_n |n_A\rangle \\ \sum_{n=0}^\infty \sqrt{n!} d_n |n_A\rangle \\ \sum_{n=0}^\infty \sqrt{n!} e_n |n_A\rangle \end{bmatrix}, \tag{5}$$

where c_n, d_n , and e_n are the expansion coefficients (proportional to probability amplitudes), respectively. Substituting this expansion into the Schrödinger equation $H_A|\Psi_A\rangle = E|\Psi_A\rangle$, we obtain

$$\begin{aligned} \sum_{n=0}^\infty \left(\omega n - \frac{g^2}{\omega} + 2\epsilon\right) \sqrt{n!} c_n |n_A\rangle + \sqrt{2}\Omega \sum_{n=0}^\infty \sqrt{n!} d_n |n_A\rangle &= E \sum_{n=0}^\infty \sqrt{n!} c_n |n_A\rangle, \\ \sum_{n=0}^\infty d_n \left[\sqrt{n!} \left(n\omega + \frac{3g^2}{\omega}\right) |n_A\rangle - 2g(\sqrt{n^2} \sqrt{(n-1)!} |(n-1)_A\rangle + \sqrt{(n+1)!} |(n+1)_A\rangle)\right] \\ + \sqrt{2}\Omega \sum_{n=0}^\infty \sqrt{n!} (c_n + e_n) |n_A\rangle &= E \sum_{n=0}^\infty \sqrt{n!} d_n |n_A\rangle, \\ \sum_{n=0}^\infty \left(\omega n - \frac{g^2}{\omega} - 2\epsilon\right) \sqrt{n!} e_n |n_A\rangle + \sqrt{2}\Omega \sum_{n=0}^\infty \sqrt{n!} d_n |n_A\rangle &= E \sum_{n=0}^\infty \sqrt{n!} e_n |n_A\rangle \end{aligned}$$

for eigenenergy E . Multiplying by the state $\langle m_A|$ from the left-hand side, we derive coupled equations of the coefficients,

$$\left(\omega m - \frac{g^2}{\omega} + 2\epsilon\right) c_m + \sqrt{2}\Omega d_m = E c_m, \tag{6}$$

$$\begin{aligned} \left(\omega m - \frac{3g^2}{\omega}\right) d_m - 2g[(m+1)d_{m+1} - d_{m-1}] \\ + \sqrt{2}\Omega(c_m + e_m) = E d_m, \end{aligned} \tag{7}$$

$$\left(\omega m - \frac{g^2}{\omega} - 2\epsilon\right) e_m + \sqrt{2}\Omega d_m = E e_m. \tag{8}$$

From Eqs. (6) and (8) one finds expressions of c_m and e_m with respect to the common coefficient d_m . Substituting these into Eq. (7) yields a recursion relation for d_m ,

$$m d_m = C_{m-1} d_{m-1} - d_{m-2},$$

where the coefficient C_m is defined as

$$C_m = \frac{1}{2g} \left[\omega m + \frac{3g^2}{\omega} - E + 2\Omega^2 \left(\frac{1}{D+2\epsilon} + \frac{1}{D-2\epsilon} \right) \right].$$

with $D = E - \omega m + g^2/\omega$. Using the initial coefficients $d_0 = 1$ and $d_1 = C_0$, the coefficients d_m can be evaluated iteratively when parameters $\{E, \omega, \epsilon, \Omega, g\}$ are specified.

In a similar way we rewrite the Hamiltonian H using operators B and B^\dagger ,

$$H_B = \begin{bmatrix} \mathcal{F}_B + 2\epsilon & \sqrt{2}\Omega & 0 \\ \sqrt{2}\Omega & \mathcal{D}_B & \sqrt{2}\Omega \\ 0 & \sqrt{2}\Omega & \mathcal{F}_B - 2\epsilon \end{bmatrix}, \quad (9)$$

where $\mathcal{F}_B = \omega B^\dagger B + 2g(B^\dagger + B) + 3g^2/\omega$ and $\mathcal{D}_B = \omega B^\dagger B - g^2/\omega$. The corresponding eigenstate $|\Psi_B\rangle$ is expressed as

$$|\Psi_B\rangle = \begin{bmatrix} \sum_{n=0}^{\infty} (-1)^n \sqrt{n!} c'_n |n_B\rangle \\ \sum_{n=0}^{\infty} (-1)^n \sqrt{n!} d'_n |n_B\rangle \\ \sum_{n=0}^{\infty} (-1)^n \sqrt{n!} e'_n |n_B\rangle \end{bmatrix},$$

where the coefficients c'_n , d'_n , and e'_n satisfy the recursion relations

$$m c'_m = \frac{\Omega}{\sqrt{2}g} d'_{m-1} + C_{m-1}^+ c'_{m-1} - c'_{m-2}, \quad (10)$$

$$m e'_m = \frac{\Omega}{\sqrt{2}g} d'_{m-1} + C_{m-1}^- e'_{m-1} - e'_{m-2}, \quad (11)$$

$$m d'_m = \frac{\sqrt{2}\Omega}{E + g^2/\omega - \omega m} (c'_m + e'_m), \quad (12)$$

with $C_m^\pm = (\omega m + 3g^2/\omega \pm 2\epsilon - E)/2g$.

In the standard BOA approach the arbitrary expansion coefficients in both wave functions $|\Psi_A\rangle$ and $|\Psi_B\rangle$ are all defined through the recurrence relation of a single coefficient [13,44,51,89,90]. To obtain a recurrence relation from Eqs. (10)–(12), we first derive initial coefficients c'_0 and e'_0 by following the approach presented in Ref. [48]. We left-multiply wave function $|\Psi_A\rangle$ by the bra-state $\langle 0_B|$, which yields relations between c'_0 (e'_0) and c_n (e_n),

$$c'_0 = e^{-2g^2/\omega} \sum_{n=0}^{\infty} c_n \left(\frac{2g}{\omega}\right)^n,$$

$$e'_0 = e^{-2g^2/\omega} \sum_{n=0}^{\infty} e_n \left(\frac{2g}{\omega}\right)^n.$$

When deriving the above expressions, we have used the relation $\langle 0_B | n_A \rangle = \frac{1}{\sqrt{n!}} \left(\frac{2g}{\omega}\right)^n e^{-2g^2/\omega^2}$. With these initial coefficients c'_0 and e'_0 the first iterations are obtained,

$$c'_1 = \frac{\Omega}{\sqrt{2}g} d'_0 + C_0^+ c'_0 \quad \text{and} \quad e'_1 = \frac{\Omega}{\sqrt{2}g} d'_0 + C_0^- e'_0,$$

which allow us to solve all expansion coefficients iteratively through Eqs. (10)–(12).

If E is a nondegenerate eigenenergy of H , the states $|\Psi_A\rangle$ and $|\Psi_B\rangle$ must differ only by a complex coefficient K , i.e., $|\Psi_A\rangle = K|\Psi_B\rangle$. Left-multiplying by the vacuum bra-state $\langle 0|$ on both sides, we obtain

$$\sum_{n=0}^{\infty} c_n e^{-g^2/2\omega^2} \left(\frac{g}{\omega}\right)^n = K \sum_{n=0}^{\infty} c'_n e^{-g^2/2\omega^2} \left(\frac{g}{\omega}\right)^n, \quad (13a)$$

$$\sum_{n=0}^{\infty} e_n e^{-g^2/2\omega^2} \left(\frac{g}{\omega}\right)^n = K \sum_{n=0}^{\infty} e'_n e^{-g^2/2\omega^2} \left(\frac{g}{\omega}\right)^n, \quad (13b)$$

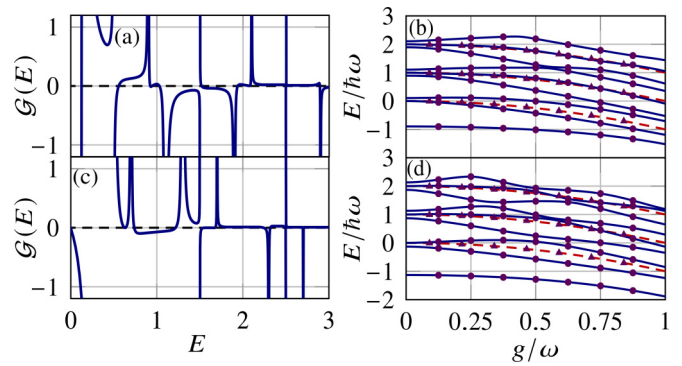


FIG. 3. (a) Braak $\mathcal{G}(E)$ function and (b) energy spectra of the TQRM for $\epsilon/\omega = 0.2$. (c) Function $\mathcal{G}(E)$ and (d) eigenspectra for $\epsilon/\omega = 0.4$. In (b) and (d) the triplet and singlet eigenenergies are denoted with solid blue lines and dashed red lines, respectively. Purple dots and triangles denote analytical results from the \mathcal{G} function and $E_{\pm}(n)$, respectively. In (a) and (c), we have set $\Omega/\omega = 0.4$ and $g/\omega = 0.5$.

where we have used relation $\sqrt{n!} \langle 0 | n_A \rangle = (-1)^n \sqrt{n!} \langle 0 | n_B \rangle = e^{-g^2/2\omega^2} (g/\omega)^n$ [44]. Cross-multiplying to eliminate the arbitrary constant K , an analytical expression for the Braak \mathcal{G} function is found,

$$\mathcal{G}(E) = \sum_{n=0}^{\infty} c_n \left(\frac{g}{\omega}\right)^n \sum_{n=0}^{\infty} e'_n \left(\frac{g}{\omega}\right)^n - \sum_{n=0}^{\infty} c'_n \left(\frac{g}{\omega}\right)^n \sum_{n=0}^{\infty} e_n \left(\frac{g}{\omega}\right)^n. \quad (14)$$

The roots of the \mathcal{G} function are used to evaluate eigenenergies of Hamiltonian (1).

Examples of the function $\mathcal{G}(E)$ are plotted in Figs. 3(a) and 3(c). Unlike the TQRM [48,51], there are no regular pole structures in our model. This results exclusively from the detuning term that breaks the symmetry in the QRM [13,91]. Roots of the $\mathcal{G}(E)$ function are evaluated numerically. In Fig. 3(b) eigenvalues of H as a function g/ω are shown. The eigenenergy obtained from the $\mathcal{G}(E)$ function agrees with the numerical diagonalization of the Hamiltonian. Anticrossings of the spectra are found at finite g . However, the ground state energy clearly separates from the first excited state. The energy gap between the ground and first excited state remains finite when $g/\omega > 1$. Increasing ϵ increases the gap too, as can be seen in Figs. 3(b) and 3(d).

V. SUBRADIANT AND SUPERRADIANT PHASES IN THE GROUND STATE

In this section we investigate properties of the ground state of the TQRM. Through mean-field calculations and numerical diagonalization of the full Hamiltonian we will show that a subradiant-to-superradiant transition can be induced by increasing g in the resonant TQRM. Phase space densities of the phonon state are symmetric but highly delocalized in the superradiant regime. The phonon state can be described by a classical mixture of coherent states $|\pm\alpha\rangle$. In the detuned TQRM we will show that the phonon state is a displaced

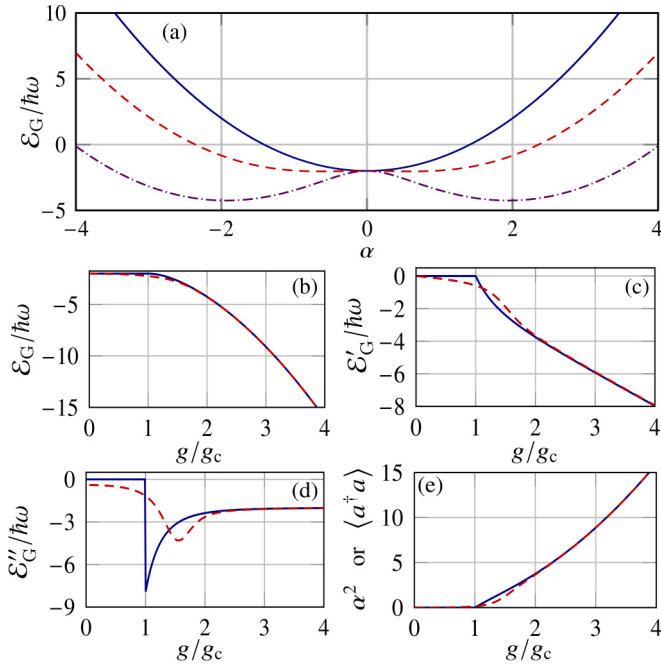


FIG. 4. (a) Mean-field energy functional \mathcal{E}_G for $g/g_c = 0.0$ (solid blue), 1.1 (dashed red), and 2.0 (dash-dotted purple). The ground-state energy is obtained at the minima of the curves. (b) The ground-state energy, (c) its first and (d) second derivatives, as well as (e) the population of the bosonic mode $\langle a^\dagger a \rangle = \alpha^2$ with respect to the coupling. Solid (dashed) lines represent the mean-field (quantum) results. In the following calculations, we scale the Hamiltonian with respect to ω and set $\Omega = \omega$.

oscillator. The subradiance disappears, as the mean phonon number is nonzero as long as $g > 0$ in the detuned TQRM.

A. Delocalized superradiant phase of the resonant TQRM

The ground state exhibits a subradiant-to-superradiant phase transition when g is larger than a critical value. We first determine the critical value within the mean-field approach. This is done by replacing operators a (a^\dagger) with their mean value α (α^*) in Hamiltonian Eq. (1). By assuming that α is real we diagonalize the Hamiltonian, and the lowest energy $\mathcal{E}_G = \omega\alpha^2 - 2\sqrt{g^2\alpha^2 + \Omega^2}$ is obtained as a function of α . In the ground state $\partial\mathcal{E}_G/\partial\alpha = 0$, which allows the definition of a critical coupling $g_c = \sqrt{\omega\Omega}$. When $g \leq g_c$, we find $\alpha = 0$. The ground state is subradiant with zero phonon occupation. When $g > g_c$, two nonzero solutions, $\alpha = \pm\alpha_0$ with $\alpha_0 = \sqrt{g^2/\omega^2 - \Omega^2/g^2}$, are obtained, indicating superradiance with a finite phonon occupation. As shown in Fig. 4(a), \mathcal{E}_G is an even function of α . Two minima are found when $g > g_c$, consistent with the above analysis.

At the mean-field level this superradiant transition is characteristic of a spontaneous symmetry breaking occurring related to a second-order transition [21,92]. Here, the energy [Fig. 4(b)] and its first derivative [Fig. 4(c)] are continuous when varying g . However, the second derivative of the ground-state energy shows a discontinuity at the critical coupling, as seen in Fig. 4(d). Both the mean-field and the exact diagonalization calculation agree well in the subradiant and

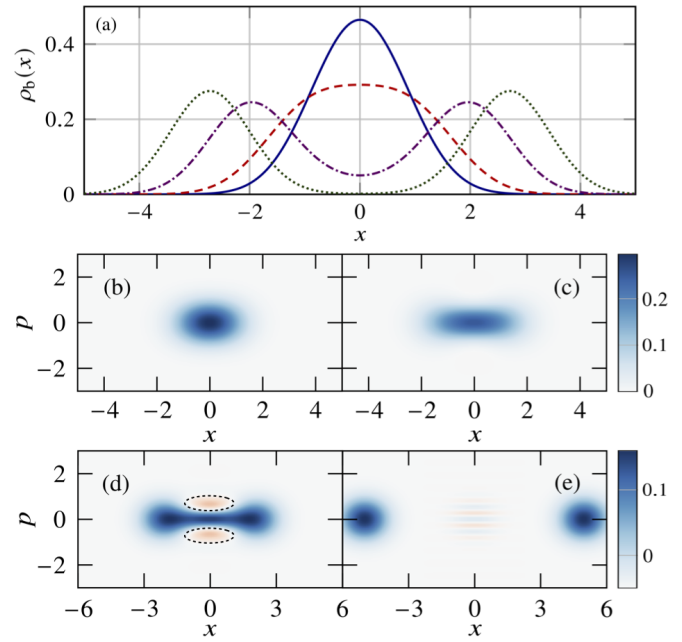


FIG. 5. (a) Density distribution $\rho_b(x)$ for couplings $g/g_c = 0.8$ (solid), $g/g_c = 1.2$ (dashed), $g/g_c = 1.6$ (dash-dotted), and $g/g_c = 2.0$ (dotted). Delocalization of the spatial density is found in the superradiant phase. The Wigner distribution $W(x, p)$ for (b) $g/g_c = 0.8$, (c) $g/g_c = 1.2$, (d) $g/g_c = 1.6$, and (e) $g/g_c = 3.5$. The Wigner distribution is stretched along the x axis when increasing g . In the superradiant regime, negative values are found, see regions marked by the ellipses in (d). In the strong coupling regime, the negative region is negligible.

superradiant phases. Around the critical point $g = g_c$, the full quantum model shows a crossover, which is different from the sharp transition in the mean-field calculation.

We now investigate the phonon states in the subradiant and superradiant phase. We are particularly interested in the phonon properties in the position representation. The position and momentum are given through phonon operators $x = l_b(a^\dagger + a)$ and $p = \frac{i}{l_b}(a^\dagger - a)$, respectively. We first numerically evaluate the reduced density matrix of the phonon $\rho_b = \text{tr}[\rho_t]$, by tracing the spin degree of freedom from the total density matrix $\rho_t = |\psi_G\rangle\langle\psi_G|$. This allows us to obtain spatial density distribution $\rho_b(x) = \langle x|\rho_b|x\rangle$ in the position representation. As shown in Fig. 5(a), the spatial density has a Gaussian profile centered at $x = 0$ in the subradiant phase. When $g \gtrsim g_c$, the density deviates from the Gaussian. It first becomes non-Gaussian around the critical value, and then splits into two separated Gaussian shapes.

The Wigner quasiprobability distribution $W(x, p)$ [93], on the other hand, exhibits distinctive features in both phases. As shown in Figs. 5(b) and 5(c), the Wigner distribution is stretched along the x axis when $g \sim g_c$. Two separate peaks are observed when $g > g_c$, depicted in Figs. 5(d) and 5(e). These peaks are centered around $x \approx \pm 2l_b\alpha_0$, similar to the spatial density shown in Fig. 5(a). The Wigner distribution is stretched horizontally (i.e., along the x axis) in the superradiant state. In certain regions, the Wigner function becomes negative, indicating the phonon cannot be described by a Gaussian state.

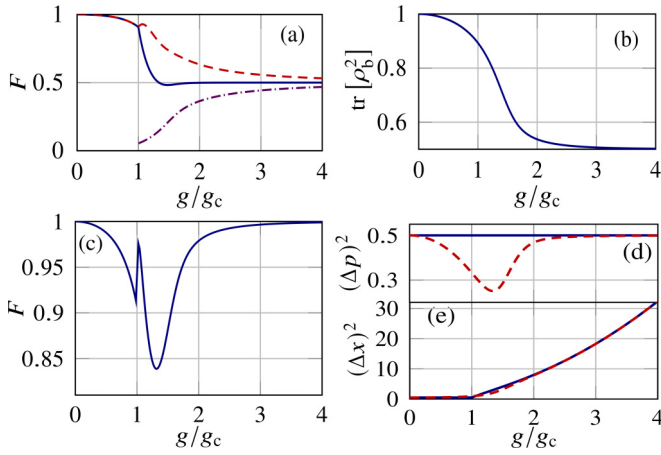


FIG. 6. (a) The Uhlmann-Jozsa fidelity F and (b) purity of the reduced density matrix ρ_b . In (a) fidelities F of ρ_b and the pure states $|\pm\alpha_0\rangle$ (solid blue), $|C_+\rangle$ (dashed red), and $|C_-\rangle$ (dash-dotted purple) are considered for $g > g_c$. When $g < g_c$, the projection to the vacuum state is examined. In (c) the fidelity between ρ_b and ρ_c is shown. (d) and (e) show the quadrature variances obtained by the mean-field (solid red) and full numerical calculations (dashed blue).

To understand the nature of the phonon state, we project ρ_b to well-defined reference states characterized by density matrix ρ_r . Their overlap is quantified by the Uhlmann-Jozsa fidelity $F = (\text{Tr} \sqrt{\sqrt{\rho_r} \rho_b \sqrt{\rho_r}})^2$ between density matrix ρ_b and ρ_r [94,95]. When $g < g_c$, the fidelity is high when $\rho_r = |0\rangle\langle 0|$, as shown in Fig. 6(a). This is a direct manifestation of the subradiance in this regime. When $g \sim g_c$, however, the fidelity becomes low in general when projecting ρ_b to $|\pm\alpha_0\rangle$ or their superpositions $|C_\pm\rangle = A_\pm(|+\alpha_0\rangle \pm |-\alpha_0\rangle)$, where $A_\pm = 1/\sqrt{2(1 \pm e^{-2\alpha_0^2})}$ is the normalization constant. This is consistent with our numerical calculation shown in Fig. 5(c), where the Wigner function exhibits negative values. In this regime, the phonon state is a non-Gaussian state, and hence cannot be accurately described by coherent states.

On the other hand, the purity of the phonon density matrix decreases rapidly with increasing g when $g \gg g_c$, as shown in Fig. 6(b). It turns out that the ρ_b becomes a classical mixture $\rho_c = \frac{1}{2}(|+\alpha_0\rangle\langle +\alpha_0| + |-\alpha_0\rangle\langle -\alpha_0|)$. When $g \gg g_c$, the corresponding fidelity F approaches unity, as shown in Fig. 6(c). Using ρ_c , we can evaluate the uncertainty of x and p analytically, $(\Delta x)^2 = (4\alpha^2 + 1)/2\omega^2$ and $(\Delta p)^2 = \omega^2[1 - (\alpha - \alpha^*)^2]/2$. As α is a real number in the mean-field calculation, this leads to $(\Delta p)^2 = \omega^2/2$. The uncertainty $(\Delta p)^2$ is therefore the same as that of the coherent state $|\pm\alpha_0\rangle$. In other words, the phonon state is strongly stretched along the x axis, while the uncertainty along the p axis remains a constant. Numerical diagonalization of the full Hamiltonian shows that $(\Delta p)^2$ only deviates from $\omega^2/2$ around $g \sim g_c$, as can be seen in Fig. 6(d).

B. Displaced superradiant phase in the detuned TQRM

We first investigate the ground state of the detuned TQRM with the mean-field approach. In Fig. 7(a) the parameter α as a function of g is shown. When increasing $g > 0$ and restricting $\epsilon > 0$, we find α is always negative and its magnitude $|\alpha|$

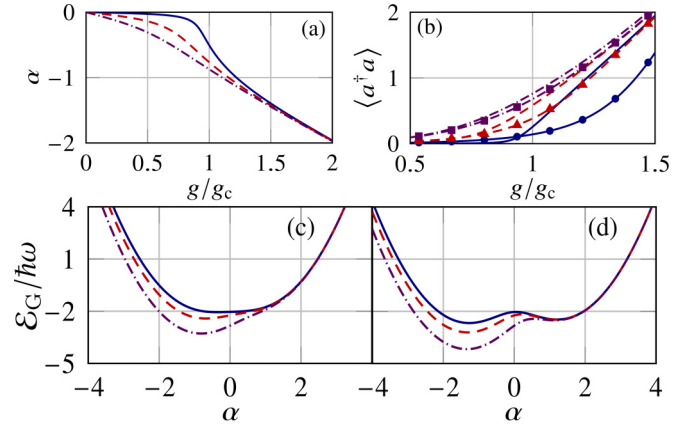


FIG. 7. (a) Mean-field α and (b) phonon population $\langle a^\dagger a \rangle$ ($|\alpha|^2$) of the resonant TQRM. In (b) the quantum and mean-field results are denoted by lines and lines with symbols, correspondingly. Energy functionals \mathcal{E}_G for (c) $g/g_c = 0.95$ and (d) $g/g_c = 1.4$ are shown. In both the subradiant and superradiant regime, minima of the energy functional locate at negative α . We have considered $\epsilon > 0$ in the calculation, where $\epsilon/\Omega = 0.2$ (solid blue), $\epsilon/\Omega = 0.5$ (dashed red), and $\epsilon/\Omega = 1.0$ (dash-dotted purple) in all the panels.

increases monotonically. This is different from the resonant TQRM, where both positive and negative branch of α are found. Another important difference is that the sharp change of α at the subradiant-superradiant transition disappears when $\epsilon > 0$. Instead, a smooth crossover emerges around $g \sim g_c$. We then calculate the mean phonon population, shown in Fig. 7(b). It is found that the crossover at $g \sim g_c$ persists. The numerical diagonalization and mean-field results deviate apparently when ϵ is small. This trend changes when ϵ is large, where the mean-field result agrees with the numerical calculation and are largely independent of ϵ . Another feature is that when ϵ is large the phonon number is nonzero as long as $g > 0$, indicating that subradiance does not exist any more. In other words, the subradiant-to-superradiant transition is removed by finite ϵ .

The negativity of α can be understood through the mean-field analysis. When $\epsilon \gg g$ and $\epsilon \gg \Omega$, the ground state energy functional is well approximated by

$$\mathcal{E}_G \approx \omega\alpha^2 + 2g\alpha - 2\epsilon.$$

When plotting \mathcal{E}_G as a function of α [see Figs. 7(c) and 7(d)] it is apparent that the minima locate at $\alpha < 0$. The value of α can be determined through solving $\partial\mathcal{E}_G/\partial\alpha = 0$. One finds ground-state energy $\mathcal{E}_G \approx -g^2/\omega - 2\epsilon$ when $\alpha_1 = -g/\omega$. This explains qualitatively why α becomes negative in the ground state.

The c.m. of the phonon density is shifted from $x = 0$ (when $\epsilon = 0$) toward $x < 0$ (when $\epsilon \neq 0$). Our numerical simulations show that the center of the spatial density [Fig. 8(a)] and Wigner distribution [Figs. 8(b) and 8(c)] are around $x \approx l_b\alpha_1$. In addition, the center of the density shifts even further when we increase coupling $|g|$ due to $x \propto -g$. This trend can be seen in Figs. 8(d)–8(f). In this regime the reduced density matrix of the phonon is well represented by the coherent state $|\alpha_1\rangle$. The Uhlmann-Jozsa fidelity between ρ_b and coherent state $|\alpha_1\rangle$ is shown in Fig. 9(a). The corresponding fidelity

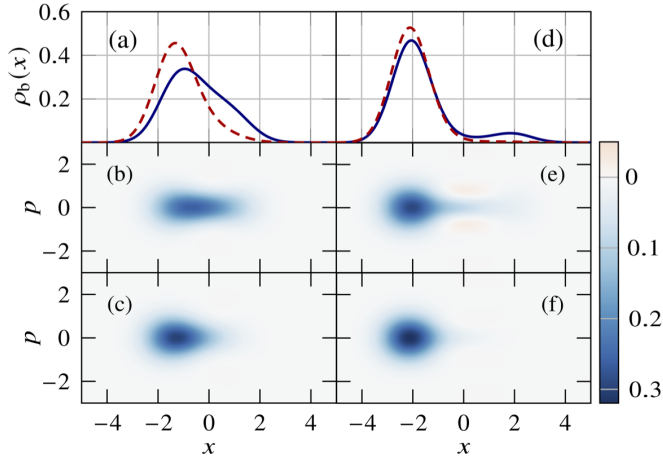


FIG. 8. Ground-state density and Wigner distribution of the detuned TQRM. When $g/g_c = 1.2$, densities for $\epsilon/\Omega = 0.2$ (solid) and 0.4 (dashed) are shown in (a). We show corresponding Wigner distribution $W(x, p)$ in (b) and (c). In (d), $g/g_c = 1.6$, and we show the corresponding distributions in (e) and (f). The density is localized when $\epsilon/\Omega = 0.1$ (solid) and $\epsilon/\Omega = 0.2$ (dashed). The corresponding Wigner distribution is shown in (e) and (f).

increases when increasing ϵ . As a result the phonon state population is well approximated by α_1^2 , which is nonnegligible even when $g < g_c$. This means that subradiance becomes impossible when $\epsilon \neq 0$, which is consistent with the numerical data shown in Fig. 7(b). The fidelity becomes relatively low around $g \sim g_c$. Importantly, the fidelity already approaches unity when $g/g_c \approx 2$ for all ϵ shown in the figure. Due to the high fidelity, we find that the purity of the phonon density matrix approaches unity, as shown in Fig. 9(b). As a result, ρ_b approaches a pure state when $\epsilon \neq 0$ and $g > g_c$. This is in sharp contrast to the resonant TQRM, where ρ_b is a mixed state in the superradiant regime.

VI. DISCUSSION AND CONCLUSION

In this work, we have shown that the TQRM can be realized with a pair of trapped Rydberg ions, in conjunction with laser-induced spin-dependent force. In this setting the single-body terms in the Hamiltonian can be controlled by tuning the laser and Paul trap electric field. In typical experiments the detuning, Rabi frequency, and trap frequency can be varied flexibly from kHz to MHz. The challenging part is to control the tripartite coupling strength g , e.g., to probe subradiant and superradiant phases. In the Rydberg ion system,

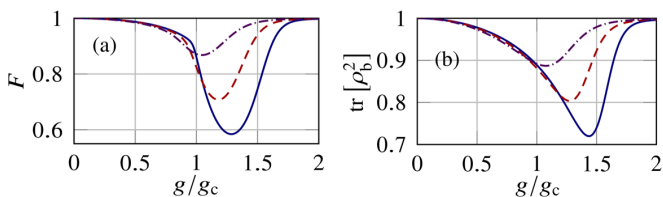


FIG. 9. (a) Uhlmann-Jozsa fidelity between ρ_b and coherent state $|\alpha_1\rangle$ (b) purity of ρ_b . In both panels, $\epsilon/\Omega = 0.1$ (solid), $\epsilon/\Omega = 0.2$ (dashed), and $\epsilon/\Omega = 0.4$ (dash-dotted).

$g/g_c = V_d(l_0)/4\sqrt{2M\Omega}$, which depends on the trap frequency implicitly through the equilibrium positions. The dipolar interaction profile is realized by using the microwave dressing scheme discussed in Ref. [74]. In this method, coherent coupling of multiple Rydberg states of different parities can shift the dipolar interaction globally, such that the interaction strength is zero at the two-ion equilibrium distance, leading to strong potential gradients that couple the two ionic spins and the phonon mode. For example, we can use the same parameters given in Ref. [74] to couple states $|50S\rangle$ and $|50P\rangle$ of $^{88}\text{Sr}^+$ ions. Considering trap frequency $\nu = 2\pi \times 1$ MHz, and $\Omega = 2\pi \times 25$ kHz, we obtain $g/g_c \approx 0.13$, which falls in the weak coupling (subradiant) regime. To access the strong coupling (superradiant) regime one can choose higher Rydberg states with $n = 80$, and tighter trap with $\nu = 2\pi \times 2.02$ MHz, which leads to $g/g_c \approx 1.04$. Hence, the tunable laser and trap parameters allows us to explore the physics of TQRM, as well as strong and collective spin-phonon coupled dynamics.

In conclusion, we have studied a TQRM where the phonon interacts with two spins simultaneously through the tripartite coupling. The Braak \mathcal{G} function is derived analytically for the TQRM, which determines the regular eigenspectra of the model. We have analyzed ground-state properties of the TQRM by varying the detuning ϵ . In the resonant case ($\epsilon = 0$), the TQRM can be reduced to the conventional QRM. In the subradiant-to-superradiant transition region, the phonon becomes a non-Gaussian state whose Wigner function exhibits negative values. In the strong coupling (superradiant) regime, it is found that the reduced density matrix of the phonon is a classical mixture of two coherent states $|\pm\alpha_0\rangle$ with equal probability. In the detuned TQRM ($\epsilon \neq 0$), the subradiance disappears for finite $g > 0$. When $g \gg g_c$, we find that ρ_b becomes a pure state $|\alpha_1\rangle$. This work opens a different way to explore exotic physics through multipartite couplings between spins and bosons. One can extend the setting to a longer ion chain, where multiple spins can couple to multiple phonon modes through the tripartite coupling [76]. Such tripartite coupling permits to create, e.g., hyperentanglement in the spin and phonon degrees of freedom simultaneously, which finds quantum information processing applications [96–102].

ACKNOWLEDGMENTS

We thank T. Yan, L. Qin, I. Straka, H. Parke, and W. S. Martins for helpful discussions. T.J.H. and W.L. acknowledge support from the EPSRC through Grant No. EP/W015641/1 and the University of Nottingham. I.L. acknowledges funding from the European Union's Horizon Europe research and innovation program under Grant Agreement No. 101046968 (BRISQ). This work was supported by the University of Nottingham and the University of Tübingen's funding as part of the Excellence Strategy of the German Federal and State Governments, in close collaboration with the University of Nottingham. This work is partially funded by the Going Global Partnerships Programme of the British Council (Contract No. IND/CONT/G/22-23/26) [103].

APPENDIX: SITE- AND SPIN-DEPENDENT STARK SHIFT

The site- and state-dependent Stark shift can be realized through applying standing wave laser light, which has been extensively studied in the quantum simulation of spin models with trapped ions. We will provide details of the realization based on the scheme in Ref. [84]. In the main text, the gradient of the dipolar interaction induces coupling between the two spins and the motion $H_d = g(\sigma_1^z \sigma_1^z + \sigma_1^z + \sigma_2^z + 1)(a + a^\dagger)$. In the following we show how to achieve site- and spin-dependent force $F_j = -g(\sigma_j^z + \frac{1}{2})(a + a^\dagger)$ to leave only the tripartite coupling.

Besides the Rydberg excitation laser, we apply another group of standing wave lasers which drive the ions from the ground state $|\downarrow\rangle = |g\rangle$ to the Rydberg state $|\uparrow\rangle = |r\rangle$ via an intermediate state $|e\rangle$ by probe and coupling fields. The level scheme is depicted in Fig. 10(a). In the case of Sr^+ ions, the wave length of the probe and coupling light are $\lambda_p = 243$ nm and $\lambda_c = 309$ nm. For concreteness, we assume the coupling light propagates along the trap z axis (or a small angle with respect to the trap axis). The propagation direction of probe light has an angle $\theta = \arccos(k_c/k_p)$ with $k_p = 2\pi/\lambda_p$ and $k_c = 2\pi/\lambda_c$, as shown in Fig. 10(b). This will ensure that the wave vectors of both fields along the trap axis are identical to $k = k_c$. The probe and coupling fields (along the trap axis) of the j th ion are given by

$$\begin{aligned}\bar{\Omega}_p^{(j)} &= \bar{\Omega}_p(e^{ikz_j} + e^{-ikz_j + i\varphi_j}) \\ \bar{\Omega}_c^{(j)} &= \bar{\Omega}_c(e^{ikz_j} + e^{-ikz_j + i\beta_j}),\end{aligned}$$

where $\bar{\Omega}_p$ and $\bar{\Omega}_c$ are amplitudes of the Rabi frequency applied on the j th ion, φ_j and β_j are the relative phase of the

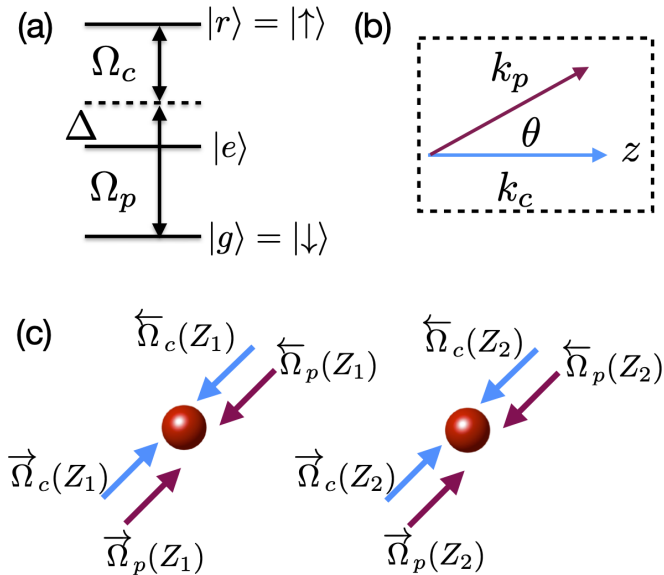


FIG. 10. (a) Level scheme. A probe light and coupling light couple the ground state to the Rydberg state resonantly via an intermediate state. (b) The relative angle between the propagation direction of the probe and coupling light. (c) Both the coupling and probe light are standing waves. The Stark shift will lead to phonon-spin coupling. By tuning the relative phase of the probe light, the spin-dependent force is realized in the Lamb-Dicke regime.

probe and coupling light, and z_j is the small deviation from the equilibrium position. The Hamiltonian that describes this interaction reads

$$H^{(j)} = \Delta\sigma_{ee}^{(j)} + (\Omega_c^{(j)}\sigma_{er}^{(j)} + \Omega_p^{(j)}\sigma_{ge}^{(j)} + \text{H.c.}), \quad (\text{A1})$$

with $\sigma_{ab}^{(j)} = |a\rangle\langle b|$ for the j th ion. Assuming both fields are weak and $\Delta \gg \Omega_c^{(j)}, \Omega_p^{(j)}$, state $|e\rangle$ is adiabatically eliminated. We obtain an effective Hamiltonian between state $|g\rangle$ and $|r\rangle$,

$$\begin{aligned}H_e^{(j)} &= -\frac{|\Omega_c^{(j)}|^2}{\Delta}\sigma_{rr}^{(j)} - \frac{|\Omega_p^{(j)}|^2}{\Delta}\sigma_{gg}^{(j)} \\ &\quad - \left(\frac{\Omega_p^{(j)}\Omega_c^{(j)}}{\Delta}\sigma_{rg}^{(j)} + \text{H.c.} \right).\end{aligned} \quad (\text{A2})$$

Following the scheme in Ref. [84], we now show how to realize the site-dependent force. In our setting, the relative phase of the standing wave fields will be different for the first and second ion, while other parameters are the same. We will set the phase of the first ion to be $\varphi_1 = -\beta_1 = -\frac{\pi}{2}$. The Rabi frequencies are given by

$$\begin{aligned}\Omega_p^{(1)} &= \Omega_p(e^{ikz_1} - ie^{-ikz_1}), \\ \Omega_c^{(1)} &= \bar{\Omega}_c(e^{ikz_1} + ie^{-ikz_1}).\end{aligned}$$

In the Lamb-Dicke regime, we Taylor expand the ionic coordinate around the equilibrium position. The state-dependent Stark shifts are obtained,

$$\begin{aligned}\frac{|\Omega_p^{(1)}|^2}{\bar{\Omega}_p^2} &= 2 - 2\sin(2kz_1) \\ &\approx 2 - 2\sqrt{2}\eta(a + a^\dagger) - 2\sqrt{2}\eta_{\text{c.m.}}(a_{\text{c.m.}} + a_{\text{c.m.}}^\dagger), \\ \frac{|\Omega_c^{(1)}|^2}{\bar{\Omega}_c^2} &= 2 + 2\sin(2kz_1) \\ &\approx 2 + 2\sqrt{2}\eta(a + a^\dagger) + 2\sqrt{2}\eta_{\text{c.m.}}(a_{\text{c.m.}} + a_{\text{c.m.}}^\dagger), \\ \frac{\Omega_p^{(1)}\Omega_c^{(1)}}{\bar{\Omega}_p\bar{\Omega}_c} &= 2\cos(2kz_1) \approx 2,\end{aligned}$$

where η and $\eta_{\text{c.m.}}$ are the Lamb-Dicke parameter of the breathing and c.m. modes. In the above equations, we have considered the linear order terms as allowed in the Lamb-Dicke regime.

In this regime, the site-dependent Stark shift F_1 considered in the main text is realized when the Rabi frequencies $\bar{\Omega}_p^2 = \frac{\Delta}{4\sqrt{2}\eta}g$, and $\bar{\Omega}_c^2 = \frac{3\Delta}{4\sqrt{2}\eta}g$. The effective Hamiltonian of the first ion becomes

$$\begin{aligned}H_e^{(1)} &= -g(a + a^\dagger)\left(\sigma_1^z + \frac{1}{2}\right) - g\sigma_1^x - \frac{g}{2\sqrt{2}\eta}(\sigma_1^z + 2) \\ &\quad - g\sqrt{3}(a_{\text{c.m.}} + a_{\text{c.m.}}^\dagger)\left(\sigma_1^z + \frac{1}{2}\right).\end{aligned} \quad (\text{A3})$$

The phases of the second ion are $\varphi_1 = -\beta_1 = \frac{\pi}{2}$. This choice of the phase is necessary as the breathing mode vector

has opposite signs for the two ions. With this phase, one carries out same calculations and obtains the Hamiltonian of the second ion,

$$H_e^{(2)} = -g(a + a^+) \left(\sigma_2^z + \frac{1}{2} \right) - g\sigma_2^x - \frac{g}{2\sqrt{2}\eta} (\sigma_2^z + 2) + g\sqrt{3}(a_{\text{c.m.}} + a_{\text{c.m.}}^\dagger) \left(\sigma_2^z + \frac{1}{2} \right). \quad (\text{A4})$$

Combining Eqs. (A3) and (A4), the total Hamiltonian becomes

$$H_e = -g(a + a^+) (\sigma_1^z + \sigma_2^z + 1) - g(\sigma_1^x + \sigma_2^x) - \frac{g}{2\sqrt{2}\eta} (\sigma_1^z + \sigma_2^z + 4) + g\sqrt{3}(a_{\text{c.m.}} + a_{\text{c.m.}}^\dagger) (\sigma_2^z - \sigma_1^z). \quad (\text{A5})$$

On the right-hand side of the Hamiltonian (A5), the first term gives the required tripartite coupling. The second and third term will contribute to the overall single-spin terms in Hamiltonian (1), where the constant term will not affect the dynamics. The last term, on the other hand, should be eliminated, as it could mix different symmetry sectors. This can be achieved by cooling the c.m. mode in the zero-phonon state $|0\rangle_{\text{c.m.}}$ [104], (or other Fock state $|n\rangle_{\text{c.m.}}$) such that $\langle 0|(a_{\text{c.m.}} + a_{\text{c.m.}}^\dagger)|0\rangle_{\text{c.m.}} = 0$. Alternatively, one could apply the dynamical decoupling scheme [105] to decouple the c.m. mode from the dynamics. As a result, tripartite coupling can be achieved.

-
- [1] I. I. Rabi, On the process of space quantization, *Phys. Rev.* **49**, 324 (1936).
- [2] M. O. Scully and M. S. Zubairy, *Quantum Optics* (Cambridge University Press, Cambridge, 1997).
- [3] A. Burger, L. C. Kwek, and D. Poletti, Digital quantum simulation of the spin-boson model under Markovian open-system dynamics, *Entropy* **24**, 1766 (2022).
- [4] M. Hirokawa, The Rabi model gives off a flavor of spontaneous SUSY breaking, *Quantum Stud.: Math. Found.* **2**, 379 (2015).
- [5] M.-L. Cai, Y.-K. Wu, Q.-X. Mei, W.-D. Zhao, Y. Jiang, L. Yao, L. He, Z.-C. Zhou, and L.-M. Duan, Observation of supersymmetry and its spontaneous breaking in a trapped ion quantum simulator, *Nat. Commun.* **13**, 3412 (2022).
- [6] T. E. Lee and Y. N. Joglekar, \mathcal{PT} -symmetric Rabi model: Perturbation theory, *Phys. Rev. A* **92**, 042103 (2015).
- [7] X. Lu, J.-K. Shi, H. Li, L.-B. Fan, V. Mangazeev, Z.-M. Li, and M. T. Batchelor, \mathcal{PT} -symmetric quantum Rabi model, *Phys. Rev. A* **108**, 053712 (2023).
- [8] S. Ashhab and F. Nori, Qubit-oscillator systems in the ultrastrong-coupling regime and their potential for preparing nonclassical states, *Phys. Rev. A* **81**, 042311 (2010).
- [9] C. Leroux, L. C. G. Govia, and A. A. Clerk, Simple variational ground state and pure-cat-state generation in the quantum Rabi model, *Phys. Rev. A* **96**, 043834 (2017).
- [10] A. Frisk Kockum, A. Miranowicz, S. De Liberato, S. Savasta, and F. Nori, Ultrastrong coupling between light and matter, *Nat. Rev. Phys.* **1**, 19 (2019).
- [11] A. Le Boité, Theoretical methods for ultrastrong light-matter interactions, *Adv. Quantum Technol.* **3**, 1900140 (2020).
- [12] E. K. Irish and A. D. Armour, Defining the semiclassical limit of the quantum Rabi Hamiltonian, *Phys. Rev. Lett.* **129**, 183603 (2022).
- [13] D. Braak, Integrability of the Rabi model, *Phys. Rev. Lett.* **107**, 100401 (2011).
- [14] B. R. Judd, Exact solutions to a class of Jahn-Teller systems, *J. Phys. C: Solid State Phys.* **12**, 1685 (1979).
- [15] A. J. Maciejewski, M. Przybylska, and T. Stachowiak, How to calculate spectra of Rabi and related models, [arXiv:1210.1130](https://arxiv.org/abs/1210.1130).
- [16] D. Braak, A generalized G -function for the quantum Rabi model, *Ann. Phys.* **525**, L23 (2013).
- [17] A. Moroz, On solvability and integrability of the Rabi model, *Ann. Phys.* **338**, 319 (2013).
- [18] H. Zhong, Q. Xie, M. T. Batchelor, and C. Lee, Analytical eigenstates for the quantum Rabi model, *J. Phys. A: Math. Theor.* **46**, 415302 (2013).
- [19] H. Zhong, Q. Xie, X. Guan, M. T. Batchelor, K. Gao, and C. Lee, Analytical energy spectrum for hybrid mechanical systems, *J. Phys. A: Math. Theor.* **47**, 045301 (2014).
- [20] Q. Xie, H. Zhong, M. T. Batchelor, and C. Lee, The quantum Rabi model: Solution and dynamics, *J. Phys. A: Math. Theor.* **50**, 113001 (2017).
- [21] M.-J. Hwang, R. Puebla, and M. B. Plenio, Quantum phase transition and universal dynamics in the Rabi model, *Phys. Rev. Lett.* **115**, 180404 (2015).
- [22] S. Felicetti and A. Le Boité, Universal spectral features of ultrastrongly coupled systems, *Phys. Rev. Lett.* **124**, 040404 (2020).
- [23] Y. Wang, Y. Su, M. Liu, and W.-L. You, Entanglement measures in the quantum Rabi model, *Phys. A: Stat. Mech. Appl.* **556**, 124792 (2020).
- [24] Y.-T. Yang and H.-G. Luo, Characterizing superradiant phase of the quantum Rabi model, *Chin. Phys. Lett.* **40**, 020502 (2023).
- [25] D. Lv, S. An, Z. Liu, J.-N. Zhang, J. S. Pedernales, L. Lamata, E. Solano, and K. Kim, Quantum simulation of the quantum Rabi model in a trapped ion, *Phys. Rev. X* **8**, 021027 (2018).
- [26] M.-L. Cai, Z.-D. Liu, W.-D. Zhao, Y.-K. Wu, Q.-X. Mei, Y. Jiang, L. He, X. Zhang, Z.-C. Zhou, and L.-M. Duan, Observation of a quantum phase transition in the quantum Rabi model with a single trapped ion, *Nat. Commun.* **12**, 1126 (2021).
- [27] J. M. Raimond, M. Brune, and S. Haroche, Manipulating quantum entanglement with atoms and photons in a cavity, *Rev. Mod. Phys.* **73**, 565 (2001).

- [28] A. Wallraff, D. I. Schuster, A. Blais, L. Frunzio, R.-S. Huang, J. Majer, S. Kumar, S. M. Girvin, and R. J. Schoelkopf, Strong coupling of a single photon to a superconducting qubit using circuit quantum electrodynamics, *Nature (London)* **431**, 162 (2004).
- [29] T. Niemczyk, F. Deppe, H. Huebl, E. P. Menzel, F. Hocke, M. J. Schwarz, J. J. Garcia-Ripoll, D. Zueco, T. Hümmer, E. Solano, A. Marx, and R. Gross, Circuit quantum electrodynamics in the ultrastrong-coupling regime, *Nat. Phys.* **6**, 772 (2010).
- [30] Z.-L. Xiang, S. Ashhab, J. Q. You, and F. Nori, Hybrid quantum circuits: Superconducting circuits interacting with other quantum systems, *Rev. Mod. Phys.* **85**, 623 (2013).
- [31] X. Gu, A. F. Kockum, A. Miranowicz, Y.-x. Liu, and F. Nori, Microwave photonics with superconducting quantum circuits, *Phys. Rep.* **718-719**, 1 (2017).
- [32] B. C. Rose, A. M. Tyryshkin, H. Riemann, N. V. Abrosimov, P. Becker, H.-J. Pohl, M. L. W. Thewalt, K. M. Itoh, and S. A. Lyon, Coherent Rabi dynamics of a superradiant spin ensemble in a microwave cavity, *Phys. Rev. X* **7**, 031002 (2017).
- [33] A. Blais, A. L. Grimsmo, S. M. Girvin, and A. Wallraff, Circuit quantum electrodynamics, *Rev. Mod. Phys.* **93**, 025005 (2021).
- [34] K. Dare, J. J. Hansen, I. Coroli, A. Johnson, M. Aspelmeyer, and U. Delić, Linear ultrastrong optomechanical interaction, [arXiv:2305.16226](https://arxiv.org/abs/2305.16226).
- [35] T. H. Stievater, X. Li, D. G. Steel, D. Gammon, D. S. Katzer, D. Park, C. Piermarocchi, and L. J. Sham, Rabi oscillations of excitons in single quantum dots, *Phys. Rev. Lett.* **87**, 133603 (2001).
- [36] D. Englund, A. Faraon, I. Fushman, N. Stoltz, P. Petroff, and J. Vučković, Controlling cavity reflectivity with a single quantum dot, *Nature (London)* **450**, 857 (2007).
- [37] S. Stuffer, P. Machnikowski, P. Ester, M. Bichler, V. M. Axt, T. Kuhn, and A. Zrenner, Two-photon Rabi oscillations in a single $\text{In}_x\text{Ga}_{1-x}\text{As}/\text{GaAs}$ quantum dot, *Phys. Rev. B* **73**, 125304 (2006).
- [38] L. Duan, Y.-F. Xie, D. Braak, and Q.-H. Chen, Two-photon Rabi model: Analytic solutions and spectral collapse, *J. Phys. A: Math. Theor.* **49**, 464002 (2016).
- [39] R. Puebla, M.-J. Hwang, J. Casanova, and M. B. Plenio, Protected ultrastrong coupling regime of the two-photon quantum Rabi model with trapped ions, *Phys. Rev. A* **95**, 063844 (2017).
- [40] S. Felicetti, D. Z. Rossatto, E. Rico, E. Solano, and P. Forn-Díaz, Two-photon quantum Rabi model with superconducting circuits, *Phys. Rev. A* **97**, 013851 (2018).
- [41] X.-H. Cheng, I. Arrazola, J. S. Pedernales, L. Lamata, X. Chen, and E. Solano, Nonlinear quantum Rabi model in trapped ions, *Phys. Rev. A* **97**, 023624 (2018).
- [42] L. Chen, X.-W. An, T.-H. Deng, and Z.-R. Zhong, Toward multimode quantum Rabi model in a strong-coupling cavity optomechanical system, *Quantum Inf. Process.* **21**, 232 (2022).
- [43] I. Travěnek, Solvability of the two-photon Rabi Hamiltonian, *Phys. Rev. A* **85**, 043805 (2012).
- [44] Q.-H. Chen, C. Wang, S. He, T. Liu, and K.-L. Wang, Exact solvability of the quantum Rabi model using Bogoliubov operators, *Phys. Rev. A* **86**, 023822 (2012).
- [45] J. Peng, Z. Ren, G. Guo, and G. Ju, Integrability and solvability of the simplified two-qubit Rabi model, *J. Phys. A: Math. Theor.* **45**, 365302 (2012).
- [46] S. A. Chilingaryan and B. M. Rodríguez-Lara, The quantum Rabi model for two qubits, *J. Phys. A: Math. Theor.* **46**, 335301 (2013).
- [47] J. Peng, Z. Ren, G. Guo, G. Ju, and X. Guo, Exact solutions of the generalized two-photon and two-qubit Rabi models, *Eur. Phys. J. D* **67**, 162 (2013).
- [48] H. Wang, S. He, L. Duan, Y. Zhao, and Q.-H. Chen, Solutions to the quantum Rabi model with two equivalent qubits, *Europhys. Lett.* **106**, 54001 (2014).
- [49] J. Peng, Z. Ren, D. Braak, G. Guo, G. Ju, X. Zhang, and X. Yuo, Solution of the two-qubit quantum Rabi model and its exceptional eigenstates, *J. Phys. A: Math. Theor.* **47**, 265303 (2014).
- [50] B. M. Rodríguez-Lara, S. A. Chilingaryan, and H. M. Moya-Cessa, Searching for structure beyond parity in the two-qubit Dicke model, *J. Phys. A: Math. Theor.* **47**, 135306 (2014).
- [51] L. Duan, S. He, and Q.-H. Chen, Concise analytic solutions to the quantum Rabi model with two arbitrary qubits, *Ann. Phys.* **355**, 121 (2015).
- [52] L. Mao, S. Huai, and Y. Zhang, The two-qubit quantum Rabi model: Inhomogeneous coupling, *J. Phys. A: Math. Theor.* **48**, 345302 (2015).
- [53] X.-M. Sun, L. Cong, H.-P. Eckle, Z.-J. Ying, and H.-G. Luo, Application of the polaron picture in the two-qubit quantum Rabi model, *Phys. Rev. A* **101**, 063832 (2020).
- [54] Z. Yan, P. Qu, B. Xu, S. Zhang, and J. Ma, Solution of two-qubit Rabi model with extended generalized rotating-wave approximation, *Mod. Phys. Lett. B* **35**, 2150213 (2021).
- [55] R. Grimaudo, A. S. M. A. de Castro, A. Messina, E. Solano, and D. Valenti, Quantum phase transitions for an integrable quantum Rabi-like model with two interacting qubits, *Phys. Rev. Lett.* **130**, 043602 (2023).
- [56] R. Grimaudo, A. A. Messina, A. Sergi, E. Solano, and D. Valenti, Thermodynamic limit in the two-qubit quantum Rabi model with spin-spin coupling, [arXiv:2310.19595v2](https://arxiv.org/abs/2310.19595v2).
- [57] P. Kirton, M. M. Roses, J. Keeling, and E. G. Dalla Torre, Introduction to the Dicke model: From equilibrium to nonequilibrium, and vice versa, *Adv. Quantum Technol.* **2**, 1800043 (2019).
- [58] H.-W. Hammer, A. Nogga, and A. Schwenk, Colloquium: Three-body forces: From cold atoms to nuclei, *Rev. Mod. Phys.* **85**, 197 (2013).
- [59] O. Katz, M. Cetina, and C. Monroe, Programmable N -body interactions with trapped ions, *PRX Quantum* **4**, 030311 (2023).
- [60] A. Goban, R. B. Hutson, G. E. Marti, S. L. Campbell, M. A. Perlin, P. S. Julienne, J. P. D'Incao, A. M. Rey, and J. Ye, Emergence of multi-body interactions in a fermionic lattice clock, *Nature (London)* **563**, 369 (2018).
- [61] C. W. S. Chang, C. Sabín, P. Forn-Díaz, F. Quijandría, A. M. Vadiraj, I. Nsanzineza, G. Johansson, and C. M. Wilson, Observation of three-photon spontaneous parametric down-conversion in a superconducting parametric cavity, *Phys. Rev. X* **10**, 011011 (2020).
- [62] F. Minganti, L. Garbe, A. Le Boité, and S. Felicetti, Non-Gaussian superradiant transition via three-body ultrastrong coupling, *Phys. Rev. A* **107**, 013715 (2023).

- [63] G. Higgins, W. Li, F. Pokorny, C. Zhang, F. Kress, C. Maier, J. Haag, Q. Bodart, I. Lesanovsky, and M. Hennrich, Single strontium Rydberg ion confined in a Paul trap, *Phys. Rev. X* **7**, 021038 (2017).
- [64] C. Zhang, F. Pokorny, W. Li, G. Higgins, A. Pöschl, I. Lesanovsky, and M. Hennrich, Submicrosecond entangling gate between trapped ions via Rydberg interaction, *Nature (London)* **580**, 345 (2020).
- [65] D. F. V. James, Quantum dynamics of cold trapped ions with application to quantum computation, *Appl. Phys. B* **66**, 181 (1998).
- [66] M. Müller, L. Liang, I. Lesanovsky, and P. Zoller, Trapped Rydberg ions: From spin chains to fast quantum gates, *New J. Phys.* **10**, 093009 (2008).
- [67] F. Schmidt-Kaler, T. Feldker, D. Kolbe, J. Walz, M. Müller, P. Zoller, W. Li, and I. Lesanovsky, Rydberg excitation of trapped cold ions: A detailed case study, *New J. Phys.* **13**, 075014 (2011).
- [68] M. Saffman, T. G. Walker, and K. Mølmer, Quantum information with Rydberg atoms, *Rev. Mod. Phys.* **82**, 2313 (2010).
- [69] W. Li and I. Lesanovsky, Electronically excited cold ion crystals, *Phys. Rev. Lett.* **108**, 023003 (2012).
- [70] W. Li, A. W. Glaetzle, R. Nath, and I. Lesanovsky, Parallel execution of quantum gates in a long linear ion chain via Rydberg mode shaping, *Phys. Rev. A* **87**, 052304 (2013).
- [71] W. Li and I. Lesanovsky, Entangling quantum gate in trapped ions via Rydberg blockade, *Appl. Phys. B* **114**, 37 (2014).
- [72] F. M. Gambetta, I. Lesanovsky, and W. Li, Exploring nonequilibrium phases of the generalized Dicke model with a trapped Rydberg-ion quantum simulator, *Phys. Rev. A* **100**, 022513 (2019).
- [73] F. M. Gambetta, C. Zhang, M. Hennrich, I. Lesanovsky, and W. Li, Long-range multibody interactions and three-body antiblockade in a trapped Rydberg ion chain, *Phys. Rev. Lett.* **125**, 133602 (2020).
- [74] F. M. Gambetta, C. Zhang, M. Hennrich, I. Lesanovsky, and W. Li, Exploring the many-body dynamics near a conical intersection with trapped Rydberg ions, *Phys. Rev. Lett.* **126**, 233404 (2021).
- [75] J. A. S. Lourenço, G. Higgins, C. Zhang, M. Hennrich, and T. Macrì, Non-Hermitian dynamics and \mathcal{PT} -symmetry breaking in interacting mesoscopic Rydberg platforms, *Phys. Rev. A* **106**, 023309 (2022).
- [76] J. W. P. Wilkinson, W. Li, and I. Lesanovsky, Spectral signatures of vibronic coupling in trapped cold atomic Rydberg systems, *arXiv:2311.16998*.
- [77] T. Feldker, P. Bachor, M. Stappel, D. Kolbe, R. Gerritsma, J. Walz, and F. Schmidt-Kaler, Rydberg excitation of a single trapped ion, *Phys. Rev. Lett.* **115**, 173001 (2015).
- [78] P. Bachor, T. Feldker, J. Walz, and F. Schmidt-Kaler, Addressing single trapped ions for Rydberg quantum logic, *J. Phys. B: At. Mol. Opt. Phys.* **49**, 154004 (2016).
- [79] G. Higgins, A Single Trapped Rydberg Ion, Ph.D. thesis, Innsbruck University and Stockholm University (2018).
- [80] A. Makhberi, J. Vogel, J. Andrijauskas, P. Bachor, J. Walz, and F. Schmidt-Kaler, Determination of quantum defect for the Rydberg P series of Ca II, *J. Phys. B: At. Mol. Opt. Phys.* **52**, 214001 (2019).
- [81] C. Zhang, Fast and Scalable Entangling Gate in Trapped Ions via Rydberg Interaction, Ph.D. thesis, Stockholm University (2020).
- [82] A. Makhberi, M. Hennrich, and F. Schmidt-Kaler, Trapped Rydberg ions: A new platform for quantum information processing, *Adv. At. Mol. Opt. Phys.* **69**, 233 (2020).
- [83] J. Andrijauskas, J. Vogel, A. Makhberi, and F. Schmidt-Kaler, Rydberg series excitation of a single trapped $^{40}\text{Ca}^+$ ion for precision measurements and principal quantum number scalings, *Phys. Rev. Lett.* **127**, 203001 (2021).
- [84] D. Porras and J. I. Cirac, Effective quantum spin systems with trapped ions, *Phys. Rev. Lett.* **92**, 207901 (2004).
- [85] X.-L. Deng, D. Porras, and J. I. Cirac, Effective spin quantum phases in systems of trapped ions, *Phys. Rev. A* **72**, 063407 (2005).
- [86] E. K. Irish, Generalized rotating-wave approximation for arbitrarily large coupling, *Phys. Rev. Lett.* **99**, 173601 (2007).
- [87] For introduction to this approach see Ref. [20]; for a mathematically rigorous definition of these Hilbert spaces and their properties see Refs. [106,107].
- [88] R. J. Glauber, Coherent and incoherent states of the radiation field, *Phys. Rev.* **131**, 2766 (1963).
- [89] L. Duan, S. He, D. Braak, and Q.-H. Chen, Solution of the two-mode quantum Rabi model using extended squeezed states, *Europhys. Lett.* **112**, 34003 (2015).
- [90] L. Duan, A unified approach to the nonlinear Rabi models, *New J. Phys.* **24**, 083045 (2022).
- [91] Y.-Q. Shi, L. Cong, and H.-P. Eckerle, Entanglement resonance in the asymmetric quantum Rabi model, *Phys. Rev. A* **105**, 062450 (2022).
- [92] X.-Y. Chen, Y.-Y. Zhang, L. Fu, and H. Zheng, Generalized coherent-squeezed-state expansion for the super-radiant phase transition, *Phys. Rev. A* **101**, 033827 (2020).
- [93] E. Wigner, On the quantum correction for thermodynamic equilibrium, *Phys. Rev.* **40**, 749 (1932).
- [94] A. Uhlmann, The “transition probability” in the state space of a $*$ -algebra, *Rep. Math. Phys.* **9**, 273 (1976).
- [95] P. E. M. F. Mendonça, R. d. J. Napolitano, M. A. Marchioli, C. J. Foster, and Y.-C. Liang, Alternative fidelity measure between quantum states, *Phys. Rev. A* **78**, 052330 (2008).
- [96] B.-C. Ren and F.-G. Deng, Hyper-parallel photonic quantum computation with coupled quantum dots, *Sci. Rep.* **4**, 4623 (2014).
- [97] B.-C. Ren and G. L. Long, Highly efficient hyperentanglement concentration with two steps assisted by quantum swap gates, *Sci. Rep.* **5**, 16444 (2015).
- [98] T. M. Graham, H. J. Bernstein, T.-C. Wei, M. Junge, and P. G. Kwiat, Superdense teleportation using hyperentangled photons, *Nat. Commun.* **6**, 7185 (2015).
- [99] F.-G. Deng, B.-C. Ren, and X.-H. Li, Quantum hyperentanglement and its applications in quantum information processing, *Sci. Bull.* **62**, 46 (2017).
- [100] X.-M. Hu, Y. Guo, B.-H. Liu, Y.-F. Huang, C.-F. Li, and G.-C. Guo, Beating the channel capacity limit for superdense coding with entangled ququarts, *Sci. Adv.* **4**, eaat9304 (2018).
- [101] X.-M. Hu, C.-X. Huang, Y.-B. Sheng, L. Zhou, B.-H. Liu, Y. Guo, C. Zhang, W.-B. Xing, Y.-F. Huang, C.-F. Li, and G.-C. Guo, Long-distance entanglement purification for quantum communication, *Phys. Rev. Lett.* **126**, 010503 (2021).

- [102] P. Scholl, A. L. Shaw, R. Finkelstein, R. B.-S. Tsai, J. Choi, and M. Endres, Erasure-cooling, control, and hyper-entanglement of motion in optical tweezers, [arXiv:2311.15580](https://arxiv.org/abs/2311.15580).
- [103] The data used to create the figures in this article can be accessed via an online repository <https://zenodo.org/records/10409685>.
- [104] F. Diedrich, J. C. Bergquist, W. M. Itano, and D. J. Wineland, Laser cooling to the zero-point energy of motion, *Phys. Rev. Lett.* **62**, 403 (1989).
- [105] P. Barthel, P. H. Huber, J. Casanova, I. Arrazola, D. Niroomand, T. Sriarunothai, M. B. Plenio, and C. Wunderlich, Robust two-qubit gates using pulsed dynamical decoupling, *New J. Phys.* **25**, 063023 (2023).
- [106] V. Bargmann, On a Hilbert space of analytic functions and an associated integral transform. Part I, *Commun. Pure Appl. Math.* **14**, 187 (1961).
- [107] I. E. Segal and G. W. Mackey, *Mathematical Problems of Relativistic Physics*, Lectures in Applied Mathematics Series Vol. 2 (American Mathematical Society, Providence, 1963).